

Composition–Structure–Activity Relationships for Palladium-Alloyed Nanocatalysts in Oxygen Reduction Reaction: An Ex-Situ/In-Situ High Energy X-ray Diffraction Study

Jinfang Wu,[†] Shiyao Shan,[†] Valeri Petkov,^{*,‡} Binay Prasai,[‡] Hannah Cronk,[†] Pharrah Joseph,[†] Jin Luo,[†] and Chuan-Jian Zhong^{*,†}

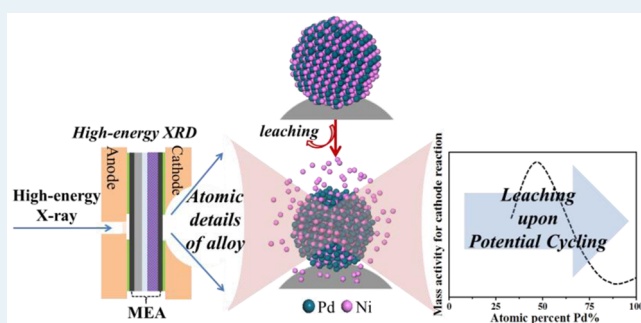
[†]Department of Chemistry, State University of New York at Binghamton, Binghamton, New York 13902, United States

[‡]Department of Physics, Central Michigan University, Mt. Pleasant, Michigan 48859, United States

S Supporting Information

ABSTRACT: Understanding how the composition and atomic-scale structure of a nanocatalyst changes when it is operated under realistic oxygen reduction reaction (ORR) conditions is essential for enabling the design and preparation of active and robust catalysts in proton exchange membrane fuel cells (PEMFCs). This report describes a study of palladium-alloyed electrocatalysts (PdNi) with different bimetallic compositions, aiming at establishing the relationship between catalyst's composition, atomic structure, and activity for ORR taking place at the cathode of an operating PEMFC. Ex-situ and in-situ synchrotron high-energy X-ray diffraction (HE-XRD) coupled to atomic pair distribution function (PDF) analysis are employed to probe the structural evolution of the catalysts under PEMFC operation conditions. The study reveals an intriguing composition–activity synergy manifested by its strong dependence on the fuel cell operation induced leaching process of base metals from the catalysts. In particular, the synergy sustains during electrochemical potential cycling in the ORR operation potential window. The alloy with Pd:Ni ratio of 50:50 atomic ratio is shown to exhibit the highest possible surface Pd–Pd and Pd–Ni coordination numbers, near which an activity is observed. The analysis of the Ni-leaching process in terms of atomic-scale structure evolution sheds further light on the activity–composition–structure correlation. The results not only show a sustainable alloy characteristic upon leaching of Ni consistent with catalytic synergy but also reveal a persistent fluctuation pattern of interatomic distances along with an atomic-level reconstruction under the ORR and fuel cell operation conditions. The understanding of this type of interatomic distance fluctuation in the catalysts in correlation with the base metal leaching and realloying mechanisms under the electrocatalytic operation conditions may have important implications in the design and preparation of catalysts with controlled activity and stability.

KEYWORDS: nanocatalysts, oxygen reduction reaction, in situ synchrotron X-ray diffraction, structural evolution, pair distribution function, interatomic distances, palladium alloy electrocatalysts



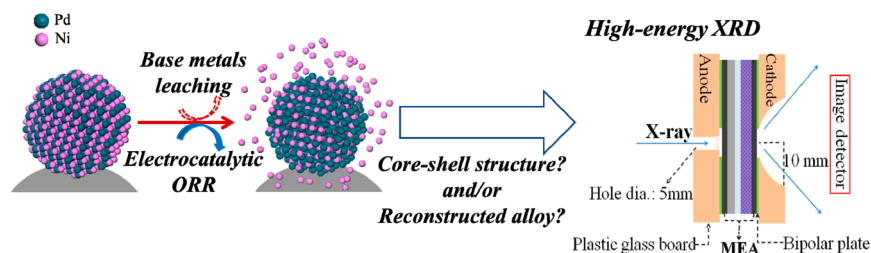
1. INTRODUCTION

In catalysis, alloying is significant in two important ways, including an ensemble effect, in which atoms in certain geometric configurations promote catalytic processes, and a ligand effect, in which modification of the electronic structure of metal species arising from hetero metal–metal bond formation favors catalytic activation.¹ In electrocatalysis for proton exchange membrane fuel cells (PEMFCs), alloying noble metals (e.g., Pt, Pd, Au, etc.) with non-noble transition metals (e.g., Co, Ni, Fe, etc.) has been an important focus in the design of catalysts for reactions taking place in fuel cells such as those for oxygen reduction reaction (ORR).^{2–5} In comparison with Pt, Pd is not only more abundant but also exhibits remarkable catalytic properties due to the fact that Pd adsorbs H and also forms compact and stable surface oxides.^{6–9} In a recent study of ORR,¹⁰ Pd–Ni alloy catalysts with different atomic ratios synthesized by a polyol method and

activated by heat treatment in a reducing atmosphere displayed surface segregation with Pd enrichment and a high activity at >50% Pd. Au-stabilized Pd–Ni core–shell nanoparticles were found to function as a stable support for a Pt monolayer for ORR.¹¹ There is also a computational study of graphene supported MPd₁₂ (M = Fe, Co, Ni, Cu, Zn, Pd) as potential ORR electrocatalysts,¹² showing that the alloying between M and Pd can enhance the cluster stability and promote ORR activity to a level comparable with that of Pt(111). First principle calculations¹³ of Pd monolayer deposited on Ni(100) for catalytic hydrogenation of ethylene showed that the surface is more active than the pure Pd(110) surface. In addition to ORR, Pd–Ni catalysts have also been studied for electrocatalytic

Received: July 26, 2015

Scheme 1. Illustration of Electrochemical Leaching of Base Metals from PdNi Alloy (i.e., Dealloying) and in-Situ HE-XRD Probing of Structural Changes of the Nanoalloy under Fuel Cell Operation Conditions



alcohol oxidation in alkaline solution,¹⁴ formic acid oxidation,¹⁵ and methanol and ethanol oxidation in alkaline media,¹⁶ demonstrating the importance of composition control to the catalytic activity enhancement. Composition control is not only important at the catalyst preparation stage but also in the catalytic reaction process, and so, it has been probed by various techniques, in particular synchrotron X-ray based techniques.^{17,18} For example, ex-situ HE-XRD coupled to atomic PDF analysis of atomic structure transformations of PtNi₆ and PtNi₃ nanoparticle catalysts after electrochemical potential cycling^{19,20} has revealed a spontaneous electrochemically induced formation of Pt–Ni particles of ordered Au₃Cu-type alloy structure (“intermetallic structure”), which is triggered by surface Ni dissolution coupled to a spontaneous residual Ni metal segregation.

In comparison with the extensively studied Pt–Ni systems for ORR,^{20–24} little has been established for Pd–Ni catalysts in understanding the relationship between the composition and electrocatalytic properties. In fact for both Pt and Pd based alloy catalysts, this understanding remains elusive, especially concerning the interrelated evolution of catalyst’s composition and atomic structure under ORR operating conditions. One of the fundamental questions for noble metal-based nanoalloys (e.g., PdNi) is do the particles adopt a core–shell type phase-segregated structure (i.e., forming a noble metal skin), and/or undergo a reconstruction involving realloying upon leaching of the base metal? For the identification of noble metal “skin” formation upon dealloying, most of the previous studies have been largely relying on high resolution TEM and EDX mapping techniques. The techniques have capability of revealing the distributions of metallic species across individual particles but have certain limitations due to limited number of nanoparticles (NPs) being examined. Since the question concerns a nanoparticle’s atomic structure and phase state, synchrotron HE-XRD/PDF carried out under ex- and in-situ ORR operating conditions appears appropriate to address the question (Scheme 1).

Recently, we have demonstrated the viability of using HE-XRD/PDF technique to probe the catalytic synergy of Pd and Ni species in Pd–Ni alloy NPs for catalytic oxidation of CO, revealing the important role of the first atomic coordination numbers and radii at nanoparticle surface.²⁵ In contrast to gas phase CO oxidation which does not involve leaching of base metals, the electrochemical reaction environment for ORR often induces dissolution of base metals from noble metal based alloy, which poses an important fundamental question on how the composition–activity synergy evolves in the electrocatalytic process of ORR. Using in-situ HE-XRD we probe the PdNi nanoalloy catalysts at atomic level during electrocatalytic process and reveal important details of their evolution under fuel cell operation conditions.

2. EXPERIMENTAL SECTION

2.1. Chemicals.

Palladium(II) acetylacetonate (Pd(acac)₂, 97%), benzyl ether (99%), oleylamine (70%), 1,2-hexadecanediol (90%), and oleic acid (99+%) were purchased from Aldrich. Nickel(II) acetylacetonate (Ni(acac)₂, >95%) were purchased from Alfa Aesar. Other chemicals such as ethanol, hexane, and potassium chloride were purchased from Fisher Scientific. Vulcan carbon XC-72 was obtained from Cabot. Pd (20% on activated carbon (Pearlman’s catalyst), unreduced, 50% water wet paste (Escat 1951, BASF Kit)) was obtained from Strem Chemicals. All gases were obtained from Airgas. All chemicals were used as received.

2.2. Synthesis and Preparation.

The synthesis of Pd_nNi_{100–n} nanoparticles followed a protocol reported previously.²⁵ Briefly, palladium(II) acetylacetonate and nickel(II) acetylacetonate were mixed in a desired molar ratio into benzyl ether solution. The composition of the Pd_nNi_{100–n} nanoparticles was controlled by the feeding molar ratio. Oleic acid and oleylamine were added as capping agents and 1,2-hexadecanediol as a reducing agent under N₂ atmosphere. The solution was purged with N₂ and heated first to 100 °C. The mixture was then heated to 220 °C and refluxed for 30 min. After the solution cooled back to room temperature, the resulting Pd–Ni NPs were precipitated out by washing and centrifugation. The preparation involved assembly of the particles on a support, and then the processing to activate the catalysts (Scheme S1, SI). Briefly, a controlled amount of PdNi nanoparticles was mixed with carbon (XC-72) in a hexane solution followed by sonication and overnight stirring. The resulting carbon supported PdNi NPs, hereafter referred as PdNi/C NPs, were collected and dried under N₂ atmosphere. The activation of Pd_nNi_{100–n}/C NPs was achieved by thermochemical processing described elsewhere.^{25–27} Typically, PdNi/C NPs were first treated at 260 °C under 20 vol % O₂ for 1 h to remove the organic capping molecules on the NP surface, and then calcined at 400 °C under 15 vol % H₂ for 2 h. Commercial Pd/C, which was treated at 400 °C under 15 vol % H₂ for 1 h, was used for comparison. The average size of commercial Pd/C NPs used was about 7 nm. The exact mass loading of catalysts was determined by thermogravimetric analysis (TGA) performed on a PerkinElmer Pyris 1-TGA. The weight loading of most PdNi/C catalysts studied in this work was within 20–37% (wt) (e.g., 37% for Pd₁₅Ni₈₅/C, Pd₆₁Ni₃₉/C and Pd₉₀Ni₁₀/C, 29% for Pd₃₀Ni₇₀/C, and 20% for Pd/C).

2.3. Characterization of Catalysts.

Inductively Coupled Plasma–Optical Emission Spectroscopy (ICP–OES). ICP–OES was used to analyze the chemical composition of the Pd–Ni NPs. The analysis was performed on a PerkinElmer 2000 DV ICP–OES instrument using a cross-flow nebulizer with the following parameters: plasma 18.0 L Ar(g)/min; auxiliary 0.3 L Ar(g)/min;

nebulizer 0.73 L Ar_(g)/min; power 1500 W; peristaltic pump rate 1.40 mL/min. Laboratory check standards were analyzed for every 6 or 12 samples, with instrument recalibration if the standards were not within $\pm 5\%$ of the initial concentration.

Transmission Electron Microscopy (TEM). High-angle annular dark-field scanning TEM (HAADF-STEM) was employed to determine the morphology of the Pd_nNi_{100-n}/C NPs and catalysts. Maps of elemental distribution in Pd–Ni NPs were obtained by energy dispersive X-ray spectroscopy (EDS). The samples were prepared by dropping cast of ethyl alcohol suspension of carbon supported nanoparticles onto a carbon-coated copper grid followed by solvent evaporation at room temperature. The measurements were performed on FEI Titan G2 80-200 Chemi-STEM electron microscope at 200 kV.

X-ray Photoelectron Spectroscopy. XPS measurements were performed using a Physical Electronics Quantum 2000 scanning ESCA microprobe. This system uses a focused monochromatic Al K α X-ray (1486.7 eV) source for excitation and a spherical section analyzer. The instrument has a 16-element multichannel detection system. The X-ray beam used was a 100 W, 100- μ m in diameter beam. It was rastered over a 1.4 mm by 0.2 mm rectangle spot on the sample. The X-ray beam was incident normal to the sample, and the X-ray detector was at 45° away from the normal. The binding energy (E_b) scale was calibrated using C 1s peak at 284.8 eV as internal standard. The percentages of individual elements detected were determined by analyzing the areas of the respective XPS peaks.

Catalytic Activity Measurement. Glassy carbon (GC) disks (geometric area: 0.196 cm²) were polished with 0.005 μ m Al₂O₃ powders. A typical suspension of the catalysts was prepared by adding 5 mg catalyst (PdNi/C) to 5 mL 0.25% Nafion solution, and sonicating for 10 min. Then 10 μ L suspension was quantitatively transferred to the surface of the polished GC disk.²⁸ Cyclic voltammetry (CV) and rotating disk electrode (RDE) measurements were performed using a microcomputer-controlled electrochemical analyzer (CHI600a, CH Instruments). The experiments were performed in three-electrode electrochemical cell at room temperature. The electrolytic solution (0.1 M HClO₄) was deaerated with high purity nitrogen before CV measurements and saturated with oxygen for RDE measurements. The potentials are given with respect to reversible hydrogen electrode (RHE).

Ex-Situ and in-Situ Synchrotron High-Energy XRD (HE-XRD). HE-XRD measurements for PEMFC cathode catalysts durability were carried out in both ex-situ ($\lambda = 0.1080$ Å) and in-situ ($\lambda = 0.1080$ Å) modes at Sector 11 of the Advanced Photon Source, Argonne National Laboratory. Ex-situ HE-XRD measurements were carried out on Pd₃₀Ni₇₀/C, Pd₆₁Ni₃₉/C, and Pd₉₀Ni₁₀/C catalysts that were subjected to cyclic potential sweeps (400, 1000, 3000, and 5000 cycles) in an electrochemical cell with N₂-saturated 0.1 M HClO₄ solution between 0.4 and 1.0 V vs RHE at a scan rate of 50 mV/s at room temperature. The catalysts were dried and collected under Ar, and then vacuum-sealed between Kapton foils. In-situ HE-XRD measurements were carried out on membrane electrode assemblies (MEAs) using Pd₃₀Ni₇₀/C (40% metal loading, 0.6 mg_{Pd}/cm²) catalyst for the cathode and Pt/C catalyst (20% Pt/C, Etek, 0.08 mg_{Pt}/cm²) for the anode. The MEAs were prepared by hot pressing the sandwich structured Nafion membrane (DuPont) and catalyst coated electrodes at 120 °C. The MEAs were tested in a custom-built fuel cell²⁹ (Scheme S2, SI) under standard catalyst's durability testing conditions (100% humidified 3.5% H₂ (in He) at a flow rate of 50 mL/min in the anode and exposing the

cathode to Ar at 75 °C). HE-XRD data was collected at intervals of 5 min while the cell was cycled in the range of 0.6–1.2 V at a scan rate of 100 mV/s for ~ 10 h amounting to about 3000 cycles.

In- and ex-situ experimental HE-XRD patterns were reduced to the so-called structure factors, $S(q)$, and then Fourier transformed to atomic PDFs $G(r)$. Note atomic PDFs $G(r)$ are experimental quantities that oscillate around zero and show positive peaks at real space distances, r , where the local atomic density $\rho(r)$ exceeds the average one ρ_o . More precisely, by definition, $G(r) = 4\pi r \rho_o [\rho(r)/\rho_o - 1]$, where $\rho(r)$ and ρ_o are the local and average atomic number density, respectively. High-energy XRD and atomic PDFs have already proven to be very efficient in studying the atomic-scale structure of nanosized materials, including metallic alloy NPs.^{30,31}

Computational Modeling. Ab-initio calculations were carried out by DFT as implemented in DMol3 program coming as a part of Materials Studio suit of programs (Accelrys Inc.).^{32,33} In the calculations, the generalized gradient approximation (GGA) with the Becke–Lee–Yang–Parr (BLYP) exchange correlation functional was used.^{34,35} The localized double numerical basis sets with polarization functions (DNP) were employed for the valence orbitals,³⁶ and effective core potential was employed to account for the core electrons of metallic species. Full geometry optimizations were performed for all model atomic configurations tested here so that all atoms were fully relaxed. The configurations included unsupported small Pd–Ni clusters. The interactions between the model atomic configurations and O₂ molecule were explored. The energy of adsorption of O₂ on the model atomic configurations was used as a measure of the strength of O₂ adsorption. It was calculated by $E_{\text{ads}} = -(E_{\text{O}_2\text{-metal}} - E_{\text{metal}} - E_{\text{O}_2})$, where, $E_{\text{O}_2\text{-metal}}$, E_{metal} , and E_{O_2} are total energy for the O₂-metal complex, the isolated atomic configuration, and the isolated O₂ molecule, respectively.³⁷

3. RESULTS AND DISCUSSION

3.1. Morphology and Composition of PdNi Nanoparticles and PdNi/C Catalysts. *Composition.* The relationship between Pd composition in Pd_nNi_{100-n} NPs and the synthetic feeding composition is shown in Figure 1. After depositing on carbon and thermal treatment, the composition of carbon-supported Pd_nNi_{100-n} (Pd₁₅Ni₈₅/C, Pd₃₀Ni₇₀/C,

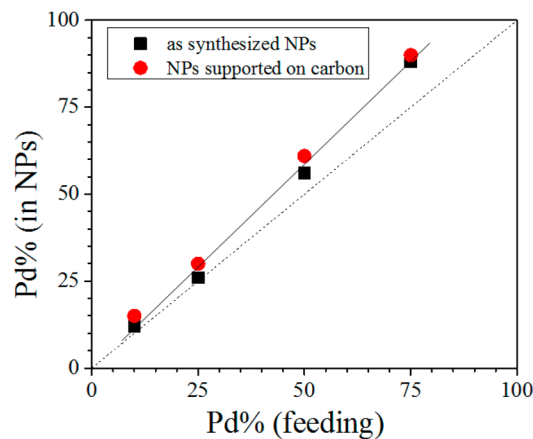


Figure 1. Plot of Pd composition in Pd_nNi_{100-n} nanoparticles (from ICP-OES analysis) vs the synthetic feeding composition. The dashed line represents a 1:1 relationship. The solid line represents the linear fitting to the NPs/C data (slope: 1.2, $R^2 = 0.997$).

Pd₆₁Ni₃₉/C, and Pd₉₀Ni₁₀/C) showed very little change in comparison with the as-synthesized NPs (Pd₁₂Ni₈₈, Pd₂₆Ni₇₄, Pd₅₆Ni₄₄, and Pd₈₈Ni₁₂) (Table S1, SI), indicating a negligible effect of the nanoparticle supporting process on the bimetallic composition. Data for the composition of Pd–Ni NPs shows a slope of 1.2, which is slightly larger than 1, indicating that the chemical composition of the binary alloy Pd–Ni NPs can be controlled well by controlling the feeding ratio of the metal precursors in the synthesis. The fact that the slope is slightly larger than one indicates that Pd is more favored than Ni in the formation of bimetallic nanoparticles.

The relative surface structure and composition of Pd_nNi_{100–n}/C NPs were also analyzed using XPS technique (Figure S1, SI). The binding energies and relative elemental ratios for Pd and Ni species in Pd–Ni NPs are shown in Table S2. Elemental ratios obtained by XPS which is sensitive to NP surface, are very close to those determined by ICP-OES, which is representative of the chemical composition of bulk NPs. The consistency between the surface and bulk composition of Pd–Ni NPs confirms the largely random alloy character of Pd_nNi_{100–n}/C nanoparticles ($n = 30, 61, \text{ and } 90$). Besides, both the Pd 3d peak and Ni 2p peak were found to shift slightly to a higher binding energy as the percentage of Ni in the nanoparticles increased. The main Ni 2p_{3/2} and 2p_{1/2} peaks were observed at 855.6 and ~861.5 eV (very weak), characteristic of oxidized Ni (+2), with a small fraction at 852.9 eV characteristic of Ni (0). Therefore, for Ni, there is not only Ni (0) but also Ni (+2) species, likely due to air exposure of the samples before XPS measurements. The O 1s peak appeared as a doublet, suggesting the presence of two types of surface oxygenated species, likely associated with the different oxidation states of Ni on NP surface. Also, XPS data show that, as Ni% in Pd_nNi_{100–n}/C increases, the oxidation peak of Ni increases.

The metal loadings in catalysts were determined by TGA (Figure S2, SI). In comparison with the nanoparticle mixed with carbon (20% metal loading) before thermal treatment, all the catalysts after thermal treatment showed an increase in metal loading because of burning of the carbon support resulting in loading rates of 37% for Pd₁₅Ni₈₅/C, Pd₆₁Ni₃₉/C and Pd₉₀Ni₁₀/C, 29% for Pd₃₀Ni₇₀/C, and 20% for Pd/C. Note, for Pd₃₀Ni₇₀/C, the degree of burning of carbon support was found to be smaller than that of other Pd–Ni nanoalloy catalysts.

Morphology. Figure 2 shows a set of typical HAADF-STEM images for carbon-supported Pd₃₀Ni₇₀ (A), Pd₆₁Ni₃₉ (B), and Pd₉₀Ni₁₀ (C) nanoparticles. The average sizes are 7.1 ± 1.1 , 5.9 ± 1.0 , and 5.4 ± 1.3 nm for Pd₃₀Ni₇₀/C, Pd₆₁Ni₃₉/C, Pd₉₀Ni₁₀/C, respectively. The subtle increase of the particle sizes, as compared with those of the as-synthesized particles, is most likely due to thermal sintering of the nanoparticles during the thermochemical treatments.

3.2. Electrocatalytic Properties for Oxygen Reduction Reaction. Activity. The carbon-supported Pd_nNi_{100–n} catalysts were examined using CV and RDE techniques for assessing their electrocatalytic activity and stability for ORR, yielding electrochemical active area (ECA), mass activity (MA), and specific activity (SA). The electrochemical measurements were performed after 30 potential cycles between 0.02 and 1.2 V (vs RHE) in N₂-saturated 0.1 M HClO₄ solution at 50 mV/s. Figure 3A shows a typical set of CV curves for catalysts with different compositions (Pd₁₅Ni₈₅/C, Pd₃₀Ni₇₀/C, Pd₆₁Ni₃₉/C, and Pd₉₀Ni₁₀/C). The voltammetric characteristics in the hydrogen adsorption/desorption region (0–0.4 V) and palladium oxidation/reduction peaks (0.6–0.8 V) showed significant

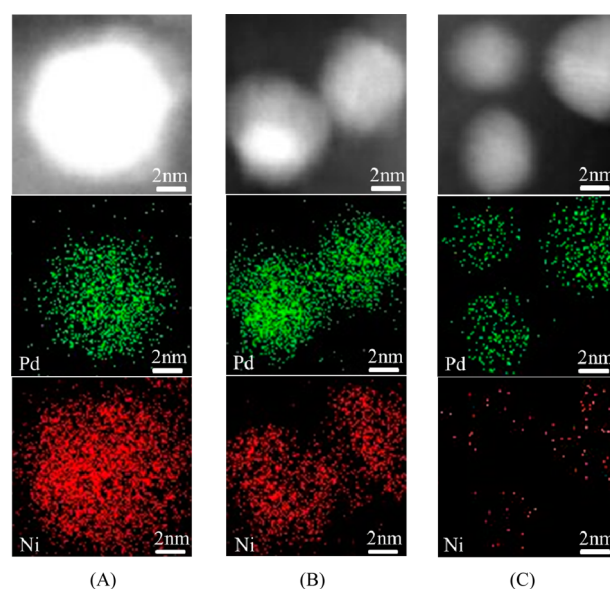


Figure 2. High-angle annular dark field scanning HAADF-STEM images (top panel) and elemental maps (middle and bottom panels) for Pd₃₀Ni₇₀/C (A), Pd₆₁Ni₃₉/C (B), and Pd₉₀Ni₁₀/C (C) nanoparticles (Ni species are in red and Pd species in green). The particle sizes are 7.1 ± 1.1 , 5.9 ± 1.0 , and 5.4 ± 1.3 nm, respectively.

differences. Pd₃₀Ni₇₀/C exhibited the largest hydrogen adsorption peak, indicative of the largest ECA value (see Figure 4), whereas Pd₆₁Ni₃₉/C showed the smallest hydrogen adsorption peak. This, as will be shown later, can be explained by the greater propensity of Ni leaching in Pd₃₀Ni₇₀/C that leads to Pd-enrichment on the surface, thus producing more hydrogen adsorption sites. The magnitude of the Pd-oxide reduction peaks showed a similar tendency with respect to the hydrogen adsorption/desorption peaks. In addition, the Pd-oxide reduction peak showed a subtle negative shift (~10 mV) for Pd₃₀Ni₇₀/C. No peak is observed for Ni/C, and there is little difference in the double-layer charging region for Pd and all Pd alloys.

In Figure 3B, the comparison of RDE curves in O₂-saturated 0.1 M HClO₄ electrolyte for catalysts with different compositions showed a clear difference in the kinetic region of ORR. Considering the fact that there were differences in Pd loading (i.e., 20%, 9.0%, 13%, 27%, and 35% for Pd/C, Pd₁₅Ni₈₅/C, Pd₃₀Ni₇₀/C, Pd₆₁Ni₃₉/C, and Pd₉₀Ni₁₀/C, respectively), changes of the kinetic currents at 0.800 V (vs RHE) for these catalysts were normalized in terms of mass activity and specific activity.

ECA values determined from the waves in the hydrogen adsorption region of CV curves are plotted as a function of NP bimetallic composition (Figure 4A), revealing a maximum value ($64 \text{ m}^2/\text{g}_{\text{Pd}}$) for $n \sim 30\%$ Pd. The mass activity data extracted from the kinetic currents (I_k) of the RDE curves at 0.800 V (vs RHE) are shown in Figure 4B. The mass activity strongly depends on the bimetallic composition. In comparison with MA for Pd/C ($0.17 \text{ A}/\text{mg}_{\text{Pd}}$), the MA for Pd₃₀Ni₇₀/C catalyst is shown to increase by ~3 times. Also, a clear trend of increasing MA with Ni% is observed. The same trend is observed with SA (Figure S3, SI). Pd₃₀Ni₇₀ catalyst shows a maximized activity for ORR, which, as will be shown later, corresponds to a composition close to a Pd:Ni ratio of 50:50 due to leaching of Ni in the nanoparticles. Similar to Pd₃₀Ni₇₀/C, Ni leaching in Pd₁₅Ni₈₅/C catalyst could lead to Pd:Ni ~ 50:50 after a certain number of electrochemical cycles, as evidenced in Figure S4 in SI. In this

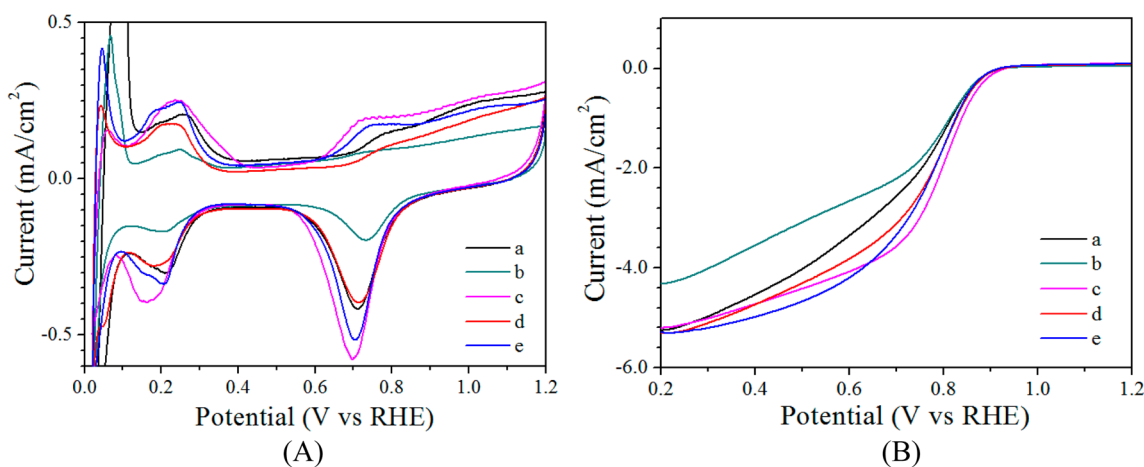


Figure 3. CV (A) and RDE (B) curves for Pd/C (a, black), Pd₁₅Ni₈₅/C (b, green), Pd₃₀Ni₇₀/C (c, pink), Pd₆₁Ni₃₉/C (d, red), and Pd₉₀Ni₁₀/C (e, blue). Electrode: Glassy carbon (0.196 cm²) inked with 10 μg catalysts. Electrolyte: 0.1 M HClO₄ saturated with N₂ for CV and 0.1 M HClO₄ saturated with O₂ for RDE. Scan rate: 50 mV/s (CV), 10 mV/s, and 1600 rpm (RDE).

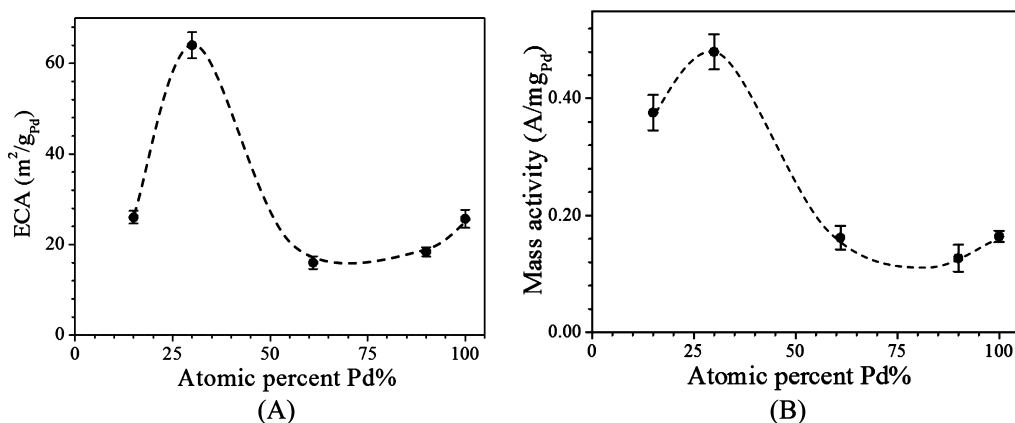


Figure 4. ECA (A) and mass activity (B) data at 0.8 V (vs RHE) for Pd/C, Pd₁₅Ni₈₅/C, Pd₃₀Ni₇₀/C, Pd₆₁Ni₃₉/C, and Pd₉₀Ni₁₀/C, as a function of Pd% in the bimetallic composition. Electrolyte: 0.1 M HClO₄ saturated with N₂ for determining ECA and 0.1 M HClO₄ saturated with O₂ for determining mass activity.

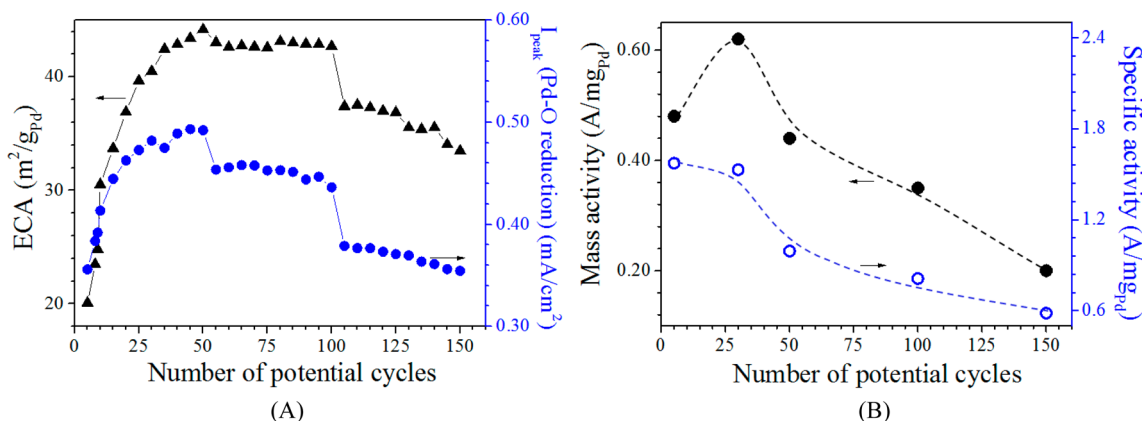


Figure 5. ECA and I_{peak} (Pd–O reduction) (A) and ORR mass activity and specific activity (B) as a function of potential cycles for Pd₃₀Ni₇₀/C (0.02–1.2 V vs RHE). Electrolyte: 0.1 M HClO₄ saturated with N₂ for determining ECA and 0.1 M HClO₄ saturated with O₂ for determining mass activity.

work we mainly focus on Pd₃₀Ni₇₀/C catalyst to illustrate the finding.

The observation of the maximum of MA is, to our knowledge, the first example of catalytic synergy of Pd and Ni species in Pd–Ni nanoalloys for ORR. Here it is worth mentioning that in a study of electrocatalytic oxidation of alcohol over Pd–Ni/C

catalysts (prepared by chemical codeposition of palladium and nickel method) in alkaline solution,¹⁴ Pd₃Ni₁/C, Pd₁Ni₁/C, and Pd₁Ni₃/C catalysts have been found equally effective in terms of MA. In a study of ORR over Pd–Ni/C in alkaline media,³⁸ the catalytic activity of PdNi (3:1)/C, PdNi (1:1)/C NPs, and PdNi (1:3)/C has been found very similar to that of Pd/C. Other

studies include DFT study on ORR activity³⁴ with an active Pd₃Ni and electrochemical oxidation of ethanol in alkaline fuel cells⁶ with an active Pd₂Ni₃. None of these studies, however, have found the catalytic synergy of Pd and Ni observed here. The synergy will be further discussed in a latter subsection.

Activity of Catalysts at Initial Stages of Potential Cycling.

The activity of the catalyst at initial stages of potential cycling in the electrocatalytic process was examined to assess the initial stability. Considering its apparent high activity, Pd₃₀Ni₇₀/C catalyst was probed in details in a standard electrochemical cell by potential cycling up to 150 cycles between 1.2 and 0.02 V vs RHE at a scan rate of 50 mV/s in N₂-saturated 0.1 M HClO₄ solution at room temperature (Figure S5, SI). In particular, changes of ECA, MA, SA, and Pd-oxide reduction after potential cycling were determined. The ECA values derived from hydrogen adsorption waves and Pd-oxide reduction peak currents are shown in Figure 5A as a function of the number of potential cycles. ECA increases initially due to removal of contaminants from NP surface. ECA and Pd-oxide reduction peak current (I_{peak}) reach a maximum after ~50 cycles and then start decreasing gradually in a stepwise manner. Similarly, the MA, as shown in Figure 5B, reaches a maximum at ~30th cycles, and then starts decreasing with further cycling. On the other hand, SA decreases gradually with cycling from its very beginning (see Figure 5B).

In view of the relatively fast leaching of Ni at the initial stage, the electrochemical characteristics in Figure 5 are indicative of dealloying of Pd–Ni NPs as a result of electrochemical cycling. To assess the degree of dealloying NP bimetallic composition was determined for several numbers of potential cycles. Figure 6

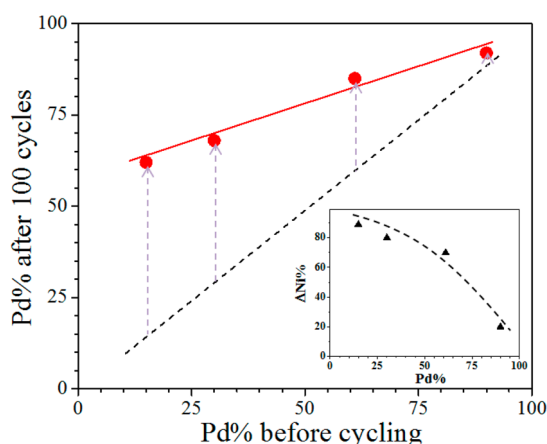


Figure 6. Comparison of changes in composition of Pd_nNi_{100–n}/C catalysts before and after 100 potential cycles from 1.2 to 0.02 V at a scan rate of 50 mV/s in N₂-saturated 0.1 M HClO₄ solution. (inset) Loss of Ni in the catalysts ($\Delta\text{Ni}\%$) after potential cycling, calculated assuming Ni is the only leaching species.

shows a representative set of data for the change in composition of Pd_nNi_{100–n}/C nanoalloy catalysts after 100 potential cycles between 0.02 and 1.2 V at 50 mV/s in N₂-saturated 0.1 M HClO₄ solution. The data shows an increase in relative Pd% in Pd_nNi_{100–n} NP catalysts with potential cycling. Likely, this increase is due to leaching of Ni species out of Pd–Ni NPs as shown in Figure 6 (see the inset). The rate of Ni leaching scales with Ni% in fresh Pd–Ni catalysts. For example, the leaching of Ni for Pd₃₀Ni₇₀/C catalysts amounts to 80% after 100 potential cycles. Clearly, the leakage rate depends on the content of Ni in

PdNi NPs in the order of Pd₃₀Ni₇₀ > Pd₆₁Ni₃₉ > Pd₉₀Ni₁₀. In other words, the more Ni, the faster the Ni leaches out.

Overall Durability. A larger number of cycles were used to study the overall durability of different compositions. This was carried out in a custom-designed electrochemical cell which allowed easy collection of the samples (Catalyst was deposited on a conductive carbon paper) for ex-situ HE-XRD and ICP analyses after various numbers of cycles. Figure 7A shows a representative set of composition data for Pd_nNi_{100–n}/C catalysts as a function of potential cycle number up to 5000 cycles (1.0–0.4 V) at 50 mV/s in N₂-saturated 0.1 M HClO₄ solution at room temperature. It is evident that as the number of cycles increases, the relative amount of Ni in the NPs gradually decreases, and the relative rate of decrease is dependent on the composition, showing the order of Pd₃₀Ni₇₀ > Pd₆₁Ni₃₉ > Pd₉₀Ni₁₀. Note that the leaching rate is consistent with those found in Figure 6.

Indeed the leaching of Ni for Pd₉₀Ni₁₀ at the first 500 cycles is insignificant, as reflected by the insignificant change of activity at the initial stage, which is consistent with the dependence of leaching rate on the content of Ni in PdNi NPs. However, there is a general agreement between the leaching and the activity. As can be seen in Figure 7B, leaching of Ni is obviously responsible for the decrease of the mass activity of the catalysts in comparison with their initial mass activities (ECA and specific activity are shown in Figure S6, SI). In particular, as the number of potential cycles increases, MA gradually decreases, with the relative rate of decrease being in the order of Pd₃₀Ni₇₀ > Pd₆₁Ni₃₉ > Pd₉₀Ni₁₀. Clearly, the potential cycling of the Pd_nNi_{100–n}/C catalysts under ORR conditions leads to leaching of Ni from the nanoalloy, and, hence, to a decrease of the electrocatalytic activity. This finding raises two important questions: (i) How does the change in NP composition affect NP atomic structure? (ii) How, in turn, do changes in the NP atomic structure affect the electrocatalytic activity or stability of nanoalloy catalysts? These two questions were addressed by ex- and in-situ HE-XRD/PDF studies, as described below.

3.3. HE-XRD/PDF Characterization. Ex-situ HE-XRD.

Having demonstrated the composition-activity synergy, it is important to know how the detailed alloying structure correlates with activity. We have recently systematically characterized the atomic structures of Pd–Ni NPs of different bimetallic compositions for gas-phase CO oxidation reaction.²⁵ The distribution of average total CNs for atoms at the surface of Pd_nNi_{100–n} NPs was extracted from 3D structure models of NPs. Based on an analysis of the distribution of CNs for atoms at the surface of Pd_nNi_{100–n} NPs as extracted from the respective 3D structure models,²⁵ we can determine the average total CNs for atoms at the surface of the NPs and relative frequency of high (CN = 7, 8, and 9) and unusually low (CN = 4 and 5) coordinated surface atoms in the NPs, which are plotted against the NP catalyst composition in Figure 8. As it can be seen in the figure, a maximum for the high-coordinated atoms and a minimum for the low-coordinated atoms is observed with Pd–Ni NPs with Pd:Ni ratio of 50:50. The maximum coincides with maximizing partial CNs (Pd–Pd and Pd–Ni) for atoms on NP surface and a minimizing of total CNs for atoms inside Pd–Ni NPs with Pd:Ni ratio of 50:50. The results indicate²⁵ that the surface of Pd–Ni catalysts with Pd:Ni ratio of 50:50 is enriched with terraces or facets in comparison with catalysts of the other compositions, which is linked to the maximum activity in the activity–composition synergy. However, this assessment does not consider the change of the composition during electrochemical process as discussed earlier.

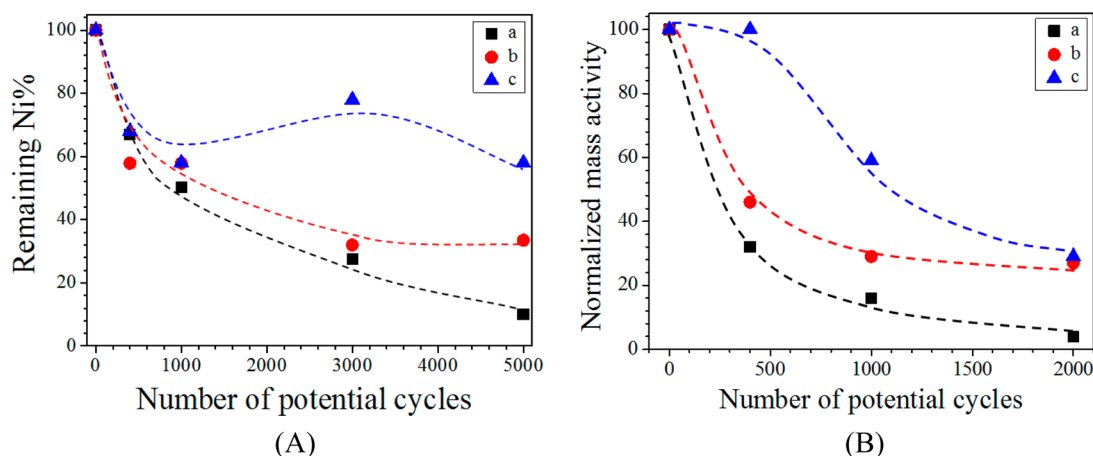


Figure 7. (A) Changes of the bimetallic composition in terms of the remaining Ni% in Pd_nNi_{100-n} NPs after different number of potential cycles in N₂-saturated 0.1 M HClO₄ solution at a scan rate of 50 mV in the potential range of 0.4–1.0 V (vs RHE) at room temperature. (B) Changes of the mass activity after different number of potential cycles as determined by RDE in 0.1 M HClO₄ saturated with O₂ (0.02–1.2 V). Catalysts: Pd₃₀Ni₇₀/C (a, black), Pd₆₁Ni₃₉/C (b, red), and Pd₉₀Ni₁₀/C (c, blue).

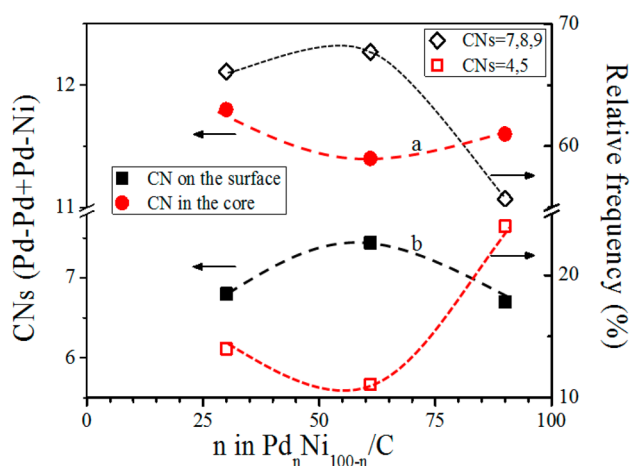


Figure 8. CNs in the core (a) and on the surface (b) (left vertical axis for closed circles and squares), and the relative frequencies corresponding to the CNs on the surface (right vertical axis for open diamonds and squares). The frequencies are in terms of high (CN = 7, 8, and 9) and low (CN = 4 and 5) coordinated surface atoms in Pd_nNi_{100-n} NPs for Pd atoms.

Having known that structure–composition correlation of the as-prepared catalysts, it is important to determine how the structure changes in ORR and fuel cell operation conditions. The structural features of Pd–Ni NP catalysts were further examined by ex-situ HE-XRD to determine the dependence of NP structure on NP bimetallic composition. Figure 9 shows a set of ex-situ atomic PDFs extracted from HE-XRD patterns (see Figure S7, SI) for Pd_nNi_{100-n} NP catalysts scraped off the electrode of an electrochemical cell after certain number of potential cycles. An accelerated durability testing protocol was used for the potential cycling (cycling in 0.1 M HClO₄ under N₂ between 0.4–1.0 V vs RHE at 50 mV/s).

Experimental atomic PDFs were approached with structure models constrained to the fcc-type structure found with bulk Pd, Ni, and Pd–Ni alloys. Refined fcc-lattice parameters (a) and goodness-of-fit indicators (R_w) are shown by each data set. The atomic PDF for Pd₃₀Ni₇₀ NPs (A) shows broad peaks, indicative of substantial atomic positional and/or chemical disorder. It may be fit with an fcc-type model though the fits are not of very high

quality due to the substantial structural disorder in Pd₃₀Ni₇₀ NPs. The atomic PDFs for both Pd₆₁Ni₃₉ (B) and Pd₉₀Ni₁₀ (C) can be fit well with an fcc-type model. In each case, the alloy characteristic of the catalyst remains after the extensive potential cycling. Apparently, the sustainability of the alloy characteristics under electrochemical cycling and the propensity of Ni-leaching imply that there is likely a realloying process occurring at the interface, the mechanism of which is further probed using in-situ HE-XRD, as described next.

In-situ HE-XRD. Having established the alloy characteristics for the catalysts under ex-situ conditions, the structural evolution and activity stability of the catalysts were examined in-situ under ORR operation condition by HE-XRD coupled to atomic PDFs analysis. Catalysts were enclosed in a custom-built fuel cell (see Scheme S2, SI). Data were taken every 3 min while the cell potential was cycled between 0.6–1.2 V at a scan rate of 100 mV/s for about 10 h. During cycling the cell was kept at 75 °C. A subset of so obtained atomic PDFs is shown in Figure 10A. Atomic PDFs for Pd₃₀Ni₇₀ catalyst after potential cycling for 400, 1000, and 3000 cycles were fit with a structure model constrained to the fcc-type crystal structure exhibited by bulk, Pd, Ni, and Pd–Ni alloys.

Refined fcc-lattice parameters are summarized in Figure 10B. Fcc-lattice parameters derived from ex-situ atomic PDFs of Pd₃₀Ni₇₀ nanocatalyst (see Figure 9A) are also shown in Figure 10B. As can be seen in Figure 10B, the “fcc-lattice parameter” of the Pd₃₀Ni₇₀ NP catalysts obtained by ex- and in-situ HE-XRD/PDFs studies follows rather similar dependence on the number of potential cycles. The dependence mirrors that of the rate of Ni leaching with number of cycles shown in Figure 7A. Also, HE-XRD derived estimates of NPs shown in Figure 10B (lower) correlate rather well with sizes determined by TEM (10.8 ± 1.2, 7.6 ± 1.0, 9.7 ± 1.5, 8.5 ± 1.8, and 12.6 ± 1.6 nm after 0, 400, 1000, 3000, and 5000 cycles; see Figure S8 SI). Interestingly, the evolution of “NP size” estimated by HE-XRD features an irregular fluctuating pattern with the number of potential cycles.

Remarkably, as can be seen in Figure 10A, the interatomic distances characteristic of the catalyst, as reflected by the positions of peaks in experimental PDFs, also evolve in a similar pattern with the number of potential cycles but with a relatively higher frequency oscillatory behavior. This indicates that atomic ordering in the Pd₃₀Ni₇₀ catalysts undergoes an “oscillatory”

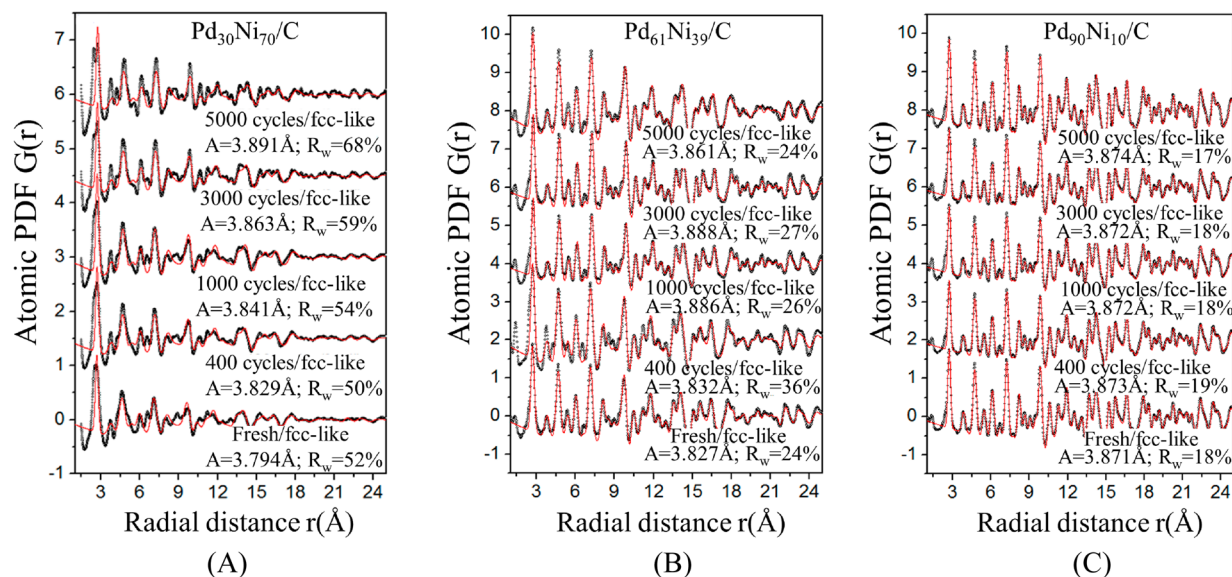


Figure 9. Ex-situ atomic PDFs data for $\text{Pd}_n\text{Ni}_{100-n}/\text{C}$ catalysts after accelerated durability test with different potential cycle numbers (potential cycling in 0.1 M HClO_4 under N_2 between 0.4–1.0 V vs RHE at 50 mV/s) where $n = 30$ (A), 61 (B), and 90 (C). The potential cycling numbers are indicated for each curve. Experimental data are given as symbols and model data as lines. Models are based on an fcc-type structure.

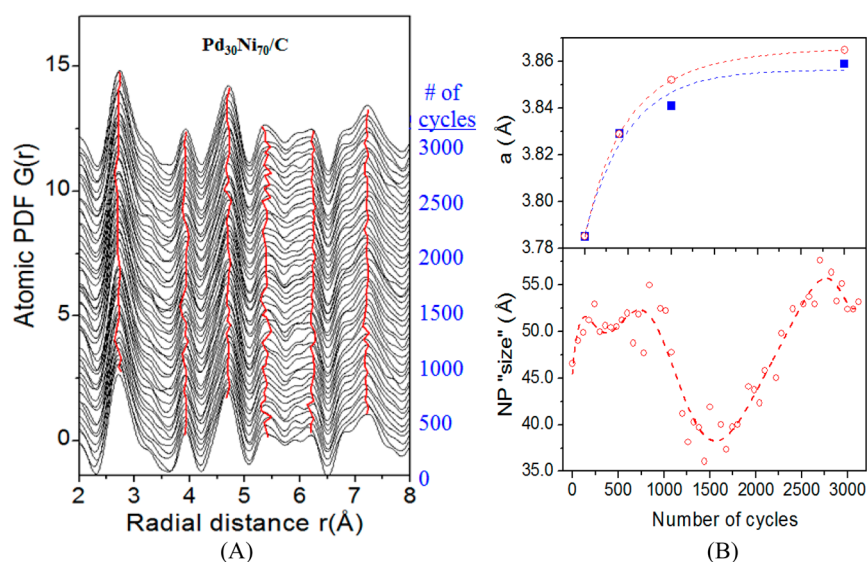


Figure 10. (A) In-situ atomic PDFs for $\text{Pd}_{30}\text{Ni}_{70}$ NPs obtained in a custom-built fuel cell cycled between 0.6–1.2 V at a scan rate of 100 mV/s. Red lines running through the PDF peaks emphasize a low-frequency fluctuation of the diffraction patterns indicative of an evolution of interatomic distances under potential cycling. (B upper) Lattice parameters of $\text{Pd}_{30}\text{Ni}_{70}$ NPs obtained from ex-situ (squares in blue) atomic PDFs of Figure 9A and in-situ atomic PDFs (open circles in red) of part A. Parameters pertain to fresh NPs and NPs which have undergone 400, 1000, and 3000 potential cycles in the fuel cell. (B lower) Effective NP size as estimated from the widths of the peaks in the respective in-situ HE-XRD patterns. Dashed lines illustrate the trends of the data points.

change, which is to our knowledge the first observation of a reconstruction of the Pd-alloyed catalysts during the potential cycling under the fuel cell operation condition. The detailed origin of the “oscillatory” behavior in the realloying and subtle resizing processes on the NP surface will be further discussed in the next subsection.

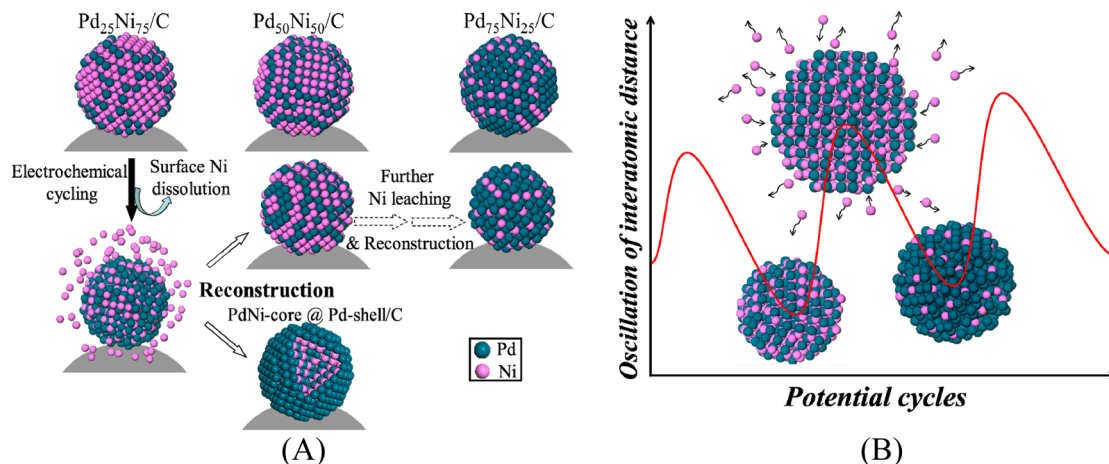
Note that there were some differences between the conditions at which ex- and in-situ HE-XRD experiments were carried out, including temperature and range of potential cycling. Yet trends of the atomic structure, catalytic activity and Ni leaching exhibited by in- and ex-situ HE-XRD data are rather similar. This observation was substantiated further by analyzing the composition of $\text{Pd}_{30}\text{Ni}_{70}$ catalyst after potential cycling for

3000 cycles in the in-situ cell. Its composition, $\text{Pd}_{81}\text{Ni}_{19}$, was found quite comparable with that determined for the same catalysts after 5000 potential cycles in an ex-situ cell.

4. MECHANISTIC CONSIDERATIONS OF COMPOSITION–STRUCTURE–ACTIVITY SYNERGY AND LEACHING–REALLOYING PROCESS

Taken together, there are two major findings: (i) nanoalloys’ composition–structure–activity synergy and (ii) nanoalloys’ lattice “oscillatory” behavior. Since both are closely linked to Ni-leaching in PdNi NPs during the electrocatalytic process, we discuss in this subsection their mechanistic details together.

Scheme 2. Idealized Models of Pd_nNi_{100-n}/C: (A) Different Bimetallic Composition (top) and Possible Mechanisms Involving Leaching of Ni from Pd₂₅Ni₇₅/C (bottom left) and a Subsequent Reconstruction of Atoms Forming Either an Ni-Poor Alloy or an PdNi Core with a Pd-Rich Shell Structure (middle and bottom right); (B) Possible Mechanism Involved in the Interatomic Distance “Oscillatory” Behavior in Terms of How the Alloy NPs Undergoes Ni-Leaching, Realloying, and Subtle Resizing on the NP Surface under the Potential Cycling



However, it is important to emphasize that these two aspects are distinctively associated with the experimental data, with one on the catalytic activity and the other on the leaching mechanism.

In Scheme 2A, models of 25/75, 50/50, and 75/25 ratios of Pd/Ni were considered to make the discussion more general. During potential cycling induced Ni-leaching process, PdNi NPs undergo oscillatory structural evolution in terms of interatomic distances (Scheme 2B) but maintain an alloy characteristic despite the reconstruction (Scheme 2A). While elemental mapping could reveal significant leaching, the result was not conclusive for two reasons: the selective or nonrepresentative sampling region in mapping and the occurrence of a realloying process under the reaction conditions. In this regard, our in-/ex-situ HE-XRD/PDF characterization provided useful information for understanding the atomic structure changes accompanying the leaching of Ni from Pd–Ni alloy catalysts during electrochemical operation under ORR condition. We consider two possible scenarios for Ni leaching out of Pd–Ni NP catalysts subjected to electrochemical cycling (Scheme 2A). One envisages reconstruction (or realloying) of the Pd–Ni nanoalloy components during leaching of Ni species. The other envisages formation of PdNi core with a Pd rich shell. While the latter is well-documented for some bimetallic nanoalloy systems, such as Pt–Ni nanoalloys,^{6,39} and others, little is known about the former. In addition to the formation of PdNi core-Pd rich shell structure, the data analysis is suggestive of the possibility of surface reconstruction or realloying of the PdNi catalysts. This assessment is inferred from the observed similarities of the dependences of the electrocatalytic activity (see Figure 4), the rate of Ni leaching (see Figure 7), and the change in the characteristic interatomic distances (see Figure 10) of the alloy catalysts on the potential cycling under the ORR or fuel cell operation condition.

To emphasize the dynamic nature of the composition dependence of the electrocatalytic activity during the potential cycling, the trends observed for the mass activity vs the bimetallic compositions determined from the as-prepared catalysts and those after the potential cycling are represented in Figure 11 (data extracted from Figures 4B and 6). Since the catalyst composition changes with cell potential cycling, it is likely that

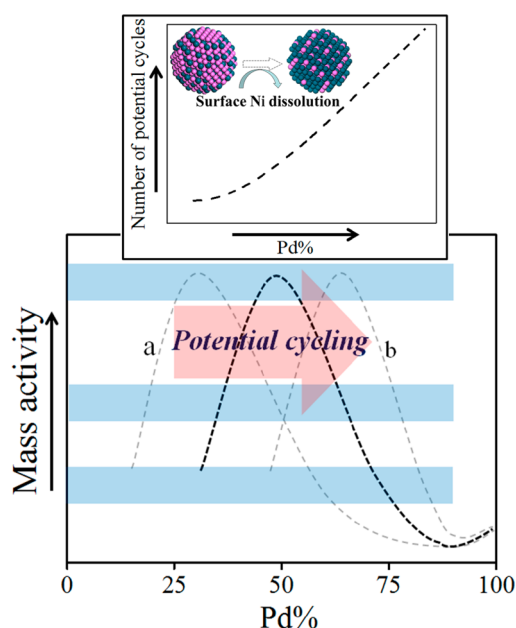


Figure 11. Dynamic illustration of the general trends observed for the mass activity vs bimetallic composition correlation for Pd_nNi_{100-n}/C catalysts before (curve a) and after extensive potential cycling (curve b). (top) Trend for the change in composition for Pd₃₀Ni₇₀/C catalyst as a result of Ni-leaching during the potential cycling.

the composition for the measured mass activity corresponds to one of the compositions in the arrow-indicated direction (see Figure 11). It is evident that Pd% in the alloy NPs changes as a result of Ni leaching during electrochemical cycling. It is important to note that activity-composition relations reported in many of precious reports were largely based on the composition before the potential cycling. In our experiments, the maximum MA at ~30% Pd observed with fresh catalysts appears to shift to somewhere >30% and <70% Pd after the catalysts have been subjected to potential cycling. Considering that the MA is measured for a composition of the catalyst in between 30% and 70% Pd, an intrinsic maximum of the catalytic

activity for Pd–Ni alloy nanoparticle catalysts for ORR near ~50% Pd is a very likely scenario.

This finding is remarkable in two ways of considerations. On one hand, if the leaching of Ni from Pd–Ni catalysts led to a complete “Pd skin” on the NP, it is unlikely for the ORR activity to display the kind of maximum observed in this work. On the other hand, it is possible that PdNi alloy NPs undergo surface reconstruction, or realloying, during leaching of Ni from the NP surface. In this regard, our ex- and in-situ HE-XRD experiments provide some important insights for assessing the structural evolution during electrochemical cycling. As shown in Figure 10B, the fcc-lattice parameter increases gradually to a plateau, indicative of an alloy phase. Furthermore, the oscillatory behavior of the interatomic distances in the NPs (see Figure 10A) and the subtle variation in NP size could be attributed to realloying of the leached Ni back to NP surface or diffusion of Ni from the core or Pd from the shell. In the MEA of the in-situ fuel cell, the leached Ni²⁺ species may remain at the vicinity of PdNi NPs and be redeposited in the potential cycling (see Scheme 2B). This type of realloying process has been observed for other NP alloy systems.⁴⁰ However, this may not be the case with the catalysts measured ex-situ since the leached Ni²⁺ ions have the possibility of diffusion into the bulk solution. It is possible that the NPs undergoes surface reconstruction in which the diffusion of the remaining Ni atoms in the alloy or the Pd atoms in the shell leads to remix. Such a surface alloying process is known as kinetically controlled self-diffusion process.⁴¹ A driving force for such diffusion would be a combination of several energetically favorable factors. In particular, Pd surface free energy (2.05 J m⁻²) is larger than Ni surface free energy (1.70 J m⁻²)^{42–44} favoring diffusion of Ni species toward NP surface. Moreover, there is a net energy stabilization by reducing the number of unsaturated bonds compared to low-coordinated Pd atoms on the surface and maximizing the number of Ni–Pd bonds.⁴⁵ Another driving force for surface realloying would be a minimization of NP surface strain. It has been shown that reducing of the intrinsic tensile strain at free NP surfaces is primarily responsible for surface alloying of bulk-immiscible Ag with Pt species.⁴⁶ Since a dealloying process would lead to shrinking of NP size, one would expect peaks in experimental atomic PDFs to broaden with progressing cycling. However, there is no apparent indication of PDF peaks broadening. Sintering of the shrunk particles could occur on the surface of the support. Size analysis of the particles scraped off carbon paper after cycling showed an indication of a slight increase in NP size (see Figure S8 SI). Further precise analysis is needed to confirm this observation.

It is the reconstructing and realloying at the Ni-leached (or dealloyed) surface that are linked to the activity-composition synergy showing a maximum at Pd% falling in between 30–70%. This type of composition-driven maximum in ORR activity was supported by DFT calculation based on small Pd–Ni cluster models yielding binding energy, d-band center, and cluster geometry (see Table S3, SI). The stability of the clusters, as reflected by the binding energy, follows the order of Pd₁Ni₃ > Pd₂Ni₂ > Pd₃Ni₁ > Pd₄. However, it does not reflect exactly the actual stability of the Pd–Ni NPs under potential cycling. Molecular chemisorption of O₂ on the model clusters was also assessed by DFT on the basis of Yeager model (Table S4 and Figure S9 SI). It was found that increasing Ni content in model clusters leads to a negative oxygen adsorption energy for a bridge site such that it shows a maximum for Pd₂Ni₂. On the other hand, the increase of the Pd–O bond distance shows a maximum (i.e.,

longest distance) for Pd₂Ni₂. DFT predicts that O–O bond distance is elongated most for Pd₁Ni₃ exhibiting two types of O₂ adsorption configurations known as Pauling and Yeager configurations (Table S4 SI). Moreover, from the partial density of states for d-orbitals in the model clusters, Pd₂Ni₂ was found to have an intermediate value of d-band center, as compared with the other model configurations, favoring ORR reaction. In summary, the preliminary DFT modeling results are supportive of the maximum ORR activity of Pd_nNi_{100–n} NPs with *n* ~ 50% Pd.

5. CONCLUSION

Results from electrocatalytic measurement of ORR, composition analysis, and ex-/in-situ HE-XRD/PDFs studies of Pd_nNi_{100–n} nanocatalysts with different bimetallic compositions have provided new insights into the correlation between the catalyst composition and the electrocatalytic properties, especially into the evolution of their composition and structure under ORR and fuel cell operation conditions. The display of a maximum activity of Pd_nNi_{100–n} catalysts with Pd% being in the range of 30–70% is linked to maximization of the surface total Pd–Pd and Pd–Ni coordination numbers based on ex-situ HE-XRD/PDF data. The leaching of Ni from the Pd–Ni catalysts under electrochemical potential cycling is shown to be linked to a structural evolution of the alloyed nanoparticle catalysts based on in-situ HE-XRD/PDF data. While maintaining the alloy characteristic upon leaching of Ni species, which is consistent with the catalytic synergy observed, the catalysts also exhibit a persistent oscillatory-type fluctuation pattern of interatomic distances along with an atomic-level reconstruction under the ORR and fuel cell operation conditions. The latter is believed to be linked to the base metal leaching and realloying mechanisms under the electrocatalytic operation condition. Clearly, the pursuit of an in-depth understanding of how this unique structural evolution correlates with the leaching of base metals in other noble metal–transition metal alloy catalysts calls for a further investigation using the in-situ high-energy XRD techniques.

■ ASSOCIATED CONTENT

📄 Supporting Information

The Supporting Information is available free of charge on the ACS Publications website at DOI: 10.1021/acscatal.5b01608.

Additional experimental details and data (PDF)

■ AUTHOR INFORMATION

Corresponding Authors

*E-mail: cjzhong@binghamton.edu (C.J.Z.).

*E-mail: petko1vg@cmich.edu (V.P.).

Notes

The authors declare no competing financial interest.

■ ACKNOWLEDGMENTS

This work was supported by the DOE-BES Grants DE-SC0006877. Work at the Advanced Photon Source was supported by DOE under Contract DE-AC02-06CH11357. Thanks are also due to Dr. Y. Ren, beamline 11-ID-C, Advanced Photon Source, for providing help with HE-XRD experiments. Jinfang Wu acknowledges the support from Chongqing University.

■ REFERENCES

- (1) Gao, F.; Goodman, D. W. *Chem. Soc. Rev.* **2012**, *41*, 8009–8020.

- (2) Loukrakpam, R.; Shan, S.; Petkov, V.; Yang, L.; Luo, J.; Zhong, C. J. *J. Phys. Chem. C* **2013**, *117*, 20715–20721.
- (3) Luo, J.; Yin, J.; Loukrakpam, R.; Wanjala, B. N.; Fang, B.; Shan, S.; Yang, L.; Ng, M. S.; Kinzler, J.; Kim, Y.-S.; Zhong, C. J. *Electroanal. Chem.* **2013**, *688*, 196–206.
- (4) Li, B.; Prakash, J. *Electrochem. Commun.* **2009**, *11*, 1162–1165.
- (5) Wanjala, B.; Fang, B.; Loukrakpam, R.; Chen, Y.; Engelhard, M.; Luo, J.; Yin, J.; Yang, L.; Shan, S.; Zhong, C. J. *ACS Catal.* **2012**, *2*, 795–806.
- (6) Shen, S. Y.; Zhao, T. S.; Xu, J. B.; Li, Y. S. *J. Power Sources* **2010**, *195*, 1001–1006.
- (7) Shao, M. H.; Liu, P.; Zhang, J. L.; Adzic, R. R. *J. Phys. Chem. B* **2007**, *111*, 6772–6775.
- (8) Shao, M. H. *J. Power Sources* **2011**, *196*, 2433–2444.
- (9) Grden, M.; Lukaszewski, M.; Jerkiewicz, G.; Czerwinski, A. *Electrochim. Acta* **2008**, *53*, 7583–7598.
- (10) Zhao, J.; Sarkar, A.; Manthiram, A. *Electrochim. Acta* **2010**, *55*, 1756–1765.
- (11) Kuttiyil, K. A.; Adzic, R. R. *Electrochim. Acta* **2013**, *110*, 267–272.
- (12) Liu, X.; Meng, C. G.; Han, Y. J. *J. Phys. Chem. C* **2013**, *117*, 1350–1357.
- (13) Filhol, J. S.; Simon, D.; Sautet, P. *J. Am. Chem. Soc.* **2004**, *126*, 3228–3233.
- (14) Jin, C. C.; Sun, X. J.; Chen, Z. D.; Dong, R. L. *Mater. Chem. Phys.* **2012**, *135*, 433–437.
- (15) Du, C. Y.; Chen, M.; Wang, W. G.; Yin, G. P. *ACS Appl. Mater. Interfaces* **2011**, *3*, 105–109.
- (16) Qi, Z.; Geng, H. R.; Wang, X. G.; Zhao, C. C.; Ji, H.; Zhang, C.; Xu, J. L.; Zhang, Z. H. *J. Power Sources* **2011**, *196*, 5823–5828.
- (17) Shan, S. Y.; Yang, L. F.; Luo, J.; Zhong, C. J. *Catal. Sci. Technol.* **2014**, *4*, 3570–3588.
- (18) Shan, S. Y.; Luo, J.; Wu, J. F.; Kang, N.; Zhao, W.; Cronk, H.; Zhao, Y.; Joseph, P.; Petkov, V.; Zhong, C. J. *RSC Adv.* **2014**, *4*, 42654–42669.
- (19) Tuae, X.; Rudi, S.; Petkov, V.; Hoell, A.; Strasser, P. *ACS Nano* **2013**, *7* (7), 5666–5674.
- (20) Gan, L.; Heggen, M.; Rudi, S.; Strasser, P. *Nano Lett.* **2012**, *12*, 5423–5430.
- (21) Debe, M. K. *Nature* **2012**, *486*, 43–51.
- (22) Gan, L.; Heggen, M.; O'Malley, R.; Theobald, B.; Strasser, P. *Nano Lett.* **2013**, *13*, 1131–1138.
- (23) Cui, C. H.; Gan, L.; Heggen, M.; Rudi, S.; Strasser, P. *Nat. Mater.* **2013**, *12*, 765–771.
- (24) Gan, L.; Heggen, M.; Strasser, P. *ECS Trans.* **2013**, *50*, 1627–1631.
- (25) Shan, S. Y.; Petkov, V.; Yang, L. F.; Luo, J.; Joseph, P.; Mayzel, D.; Prasai, B.; Wang, L. L.; Engelhard, M.; Zhong, C. J. *J. Am. Chem. Soc.* **2014**, *136*, 7140–7151.
- (26) Yin, J.; Shan, S.; Ng, M. S.; Yang, L. F.; Mott, D.; Fang, W.; Kang, N.; Luo, J.; Zhong, C. J. *Langmuir* **2013**, *29*, 9249–9258.
- (27) Luo, J.; Wang, L.; Mott, D.; Njoki, P. N.; Kariuki, N. N.; Zhong, C. J.; He, T. *J. Mater. Chem.* **2006**, *16*, 1665.
- (28) Fang, B.; Wanjala, B. N.; Hu, X.; Last, J.; Loukrakpam, R.; Yin, J.; Luo, J.; Zhong, C. J. *J. Power Sources* **2011**, *196*, 659–665.
- (29) Oxford, S. M.; Lee, P. L.; Chupas, P. J.; Chapman, K. W.; Kung, M. C.; Kung, H. H. *J. Phys. Chem. C* **2010**, *114*, 17085–17091.
- (30) Petkov, V. *Mater. Today* **2008**, *11*, 28–38.
- (31) Egami, T.; Billinge, S. J. L. *Underneath the Bragg's Peak: structural analysis of complex materials*; Pergamon: Amsterdam, 2003.
- (32) Xia, M. R.; Ding, W.; Xiong, K.; Li, L.; Qi, X. Q.; Chen, S. G.; Hu, B. S.; Wei, Z. D. *J. Phys. Chem. C* **2013**, *117*, 10581–10588.
- (33) Chang, C. R.; Wang, Y. G.; Li, J. *Nano Res.* **2011**, *4*, 131–142.
- (34) Wang, L.; Wang, Y.; Song, S. Q.; Shen, P. K. *Chin. J. Catalysis* **2009**, *30*, 433–439.
- (35) Tang, W. J.; Zhang, L.; Henkelman, G. *J. Phys. Chem. Lett.* **2011**, *2*, 1328–1331.
- (36) Li, L.; Wei, Z. D.; Chen, S. G.; Qi, X. Q.; Ding, W.; Xia, M. R.; Li, R.; Xiong, K.; Deng, Z. H.; Gao, Y. Y. *Chem. Phys. Lett.* **2012**, *539–540*, 89–93.
- (37) Wang, L.; Williams, J. I.; Lin, T.; Zhong, C. J. *Catal. Today* **2011**, *165*, 150–159.
- (38) Li, B.; Prakash, J. *Electrochem. Commun.* **2009**, *11*, 1162–1165.
- (39) Strasser, P.; Koh, S.; Anniyev, T.; Greeley, J.; More, K.; Yu, C. F.; Liu, Z. C.; Kaya, S.; Nordlund, D.; Ogasawara, H.; Toney, M. F.; Nilsson, A. *Nat. Chem.* **2010**, *2*, 454–460.
- (40) Song, T.; Yan, M.; Gao, Y.; Atrons, A.; Qian, M. *RSC Adv.* **2015**, *5*, 9574–9580.
- (41) Rizzi, M.; Furlan, S.; Peressi, M.; Baldereschi, A.; Dri, C.; Peronio, A.; Africh, C.; Lacovig, P.; Vesselli, E.; Comelli, G. *J. Am. Chem. Soc.* **2012**, *134*, 16827–16833.
- (42) Liu, G.; Clair, T. P.; Goodman, D. W. *J. Phys. Chem. B* **1999**, *103*, 8578–8582.
- (43) Nielsen, L. P.; Besenbacher, F.; Stensgaard, I.; Laegsgaard, E. L. B.; Engdahl, C.; Stoltze, P.; Jacobsen, K. W.; Norskov, J. K. *Phys. Rev. Lett.* **1993**, *71*, 754–757.
- (44) Lahr, D. L.; Ceyer, S. T. *J. Am. Chem. Soc.* **2006**, *128*, 1800–1801.
- (45) Shen, Y. G.; Yao, J.; O'Connor, D. J.; King, B. V.; MacDonald, R. J. *J. Phys.: Condens. Matter* **1996**, *8*, 4903–4918.
- (46) Batzill, M.; Koel, B. E. *Europhys. Lett.* **2003**, *64*, 70–76.